Magnon Accumulation in Chirally Coupled Magnets

Tao Yu,[1] Yu-Xiang Zhang,[2] Sanchar Sharma,[1] Xiang Zhang,[1] Yaroslav M. Blanter,[1] and Gerrit E. W. Bauer[3,1]
[1]*Kavli Institute of NanoScience, Delft University of Technology, 2628 CJ Delft, Netherlands*
[2]*Department of Physics and Astronomy, Aarhus University, 8000 Aarhus C, Denmark*
[3]*Institute for Materials Research and WPI-AIMR and CSRN, Tohoku University, Sendai 980-8577, Japan*

(Received 7 September 2019; revised manuscript received 19 December 2019; accepted 14 February 2020; published 11 March 2020)

We report strong chiral coupling between magnons and photons in microwave waveguides that contain chains of small magnets on special lines. Large magnon accumulations at one edge of the chain emerge when exciting the magnets by a phased antenna array. This mechanism holds the promise of new functionalities in nonlinear and quantum magnonics.

DOI: 10.1103/PhysRevLett.124.107202

Introduction.—The direct dipolar and exchange interactions between electron spins in condensed matter create a rich variety of magnetic order [1]. The Ruderman-Kittel-Kasuya-Yosida [2] interaction is mediated by the nonlocal exchange of mobile electrons. Magnons, the elementary excitation of the magnetic order, generate the coupling between nuclear spins [3,4]. The range of these indirect interactions is limited by the coherence length of the mediator that may be strongly affected by disorder. Photons interact only weakly with condensed matter but have long coherence lengths [5], causing interesting and potentially applicable effects on the magnetic order.

The strong exchange interaction of spins in ferromagnets generates a large magnetic dipole that couples strongly with photons in high-quality microwave cavities to create a hybridized quasiparticle—the cavity-magnon polariton [6–9]. Combining the best features of high-speed photons and long-lived magnons in low-loss materials such as yttrium iron garnet (YIG), cavity-magnon polaritons are attractive information carriers for quantum communication [6–12]. Mediated by the cavity photons with long coherence time, two magnets can be coupled coherently and tunably over macroscopic distances to create dark and bright states [10–12]. The counterpart of coherent coupling—dissipative coupling—between two local spins is described by non-Hermitian Hamiltonians [13–25], and leads to novel physics such as topological phases [18–23] with a non-Hermitian skin effect [18,19], superradiance and subradiance [26–31], as well as critical behavior beyond the standard paradigms [32–34], but has not yet been explored in magnetic systems.

In this Letter, we address the new functionalities that arise when magnetic particles couple with microwave modes that propagate only in one direction (chiral coupling). The excited state of a magnet on a line then affects only the magnets on one side without backaction. Below, we demonstrate that such chirality can be realized by special positions in a waveguide at which the precession direction of the photon magnetic field is locked to its wave vector [35–40]. Microwave devices such as nonreciprocal band rejection filters operate by placing a single ferromagnet on special points in waveguides with circular polarization [41–43]. Here we focus on the collective non-Hermitian dynamics of an ensemble of magnets as shown in Fig. 1, which is loaded with a chain of magnets close to a special line that can individually be addressed by local (coil) antennas [10]. The antenna array allows controlled excitation and detection of individual magnets as well as collective modes that is not possible by a global waveguide input and output. We predict that a chiral magnon-photon coupling in such an array leads to magnon edge states on one side of the chain. A large magnon amplitude can be generated by relatively weak excitation power, so our scheme is an alternative to parametric pumping [42,44]. We envision that similar effects occur

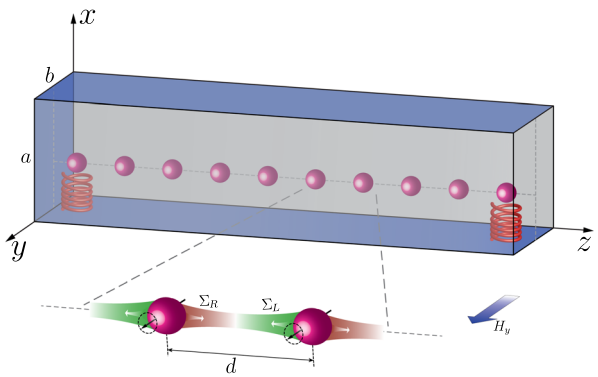

FIG. 1. Chain of magnetic spheres with period d in a microwave waveguide. The chain and waveguide are parallel to the $\hat{z}$ axis and magnetizations are oriented along $\hat{\mathbf{y}}$ by a magnetic field H_y. Every magnet interacts with all other magnets to the right (Σ_R) and left (Σ_L). Small coils attached to each magnet can excite and detect the local magnon accumulation.

when a chiral interaction between magnets is mediated by other quasiparticles such as magnons [45–47], conduction electron spins [48], and phonons [49,50]. This Letter is accompanied by a longer paper [51] that exposes the basic theory and focuses on the microwave scattering.

Formalism.—We consider a waveguide along the $\hat{\mathbf{z}}$ direction with a rectangular cross section and model it by Maxwell's equations with metallic boundary conditions. Even though the predicted effects obey classical physics, we use a quantum formalism for technical convenience as well as future research into quantum statistical effects. To this end we expand the Fano-Anderson Hamiltonian $\hat{h}_{\rm em} + \hat{h}_{\rm m} + \hat{h}_{\rm int}$ [52–54] into propagating photon operators $\hat{p}_k$ with mode number k and local magnon operators $\hat{m}_j$ with magnet index j.

The microwave magnetic-field operator $\hat{\mathbf{H}}(\mathbf{r}) = \int \mathcal{H}_k(\boldsymbol{\rho}) e^{ikz} \hat{p}_k dk/\sqrt{2\pi} + \text{H.c.}$, where $\mathcal{H}_k(\boldsymbol{\rho})$ is a waveguide eigenmode at transverse coordinate $\boldsymbol{\rho} = (x, y)$ [35] (and similarly for the electric field $\hat{\mathbf{E}}$). The electromagnetic energy $\hat{h}_{\rm em} = \int [\epsilon_0 \hat{\mathbf{E}}(\mathbf{r}) \cdot \hat{\mathbf{E}}(\mathbf{r})/2 + \mu_0 \hat{\mathbf{H}}(\mathbf{r}) \cdot \hat{\mathbf{H}}(\mathbf{r})/2] d\mathbf{r}$, where ϵ_0 and μ_0 are vacuum permittivity and permeability, then leads to the Hamiltonian $\hat{h}_{\rm em} = \int \hbar \Omega_k \hat{p}_k^\dagger \hat{p}_k dk$. We focus on the lowest transverse TE_{10} mode with dispersion $\Omega_k^2/c^2 = k^2 + (\pi/a)^2$, polarized along and uniformly distributed over the $\hat{\mathbf{y}}$ direction and with standing wavelength $2a$ in the $\hat{\mathbf{x}}$ direction (see Fig. 1 with $a > b$).

The waveguide is loaded with N identical YIG spheres with gyromagnetic ratio $-\gamma$, saturation magnetization M_s, and volume V_s at $\mathbf{r}_j = \boldsymbol{\rho} + (j-1)dz$, with $j \in \{1, 2, \ldots, N\}$, where d is the (equidistant) spacing between the spheres. The submillimeter spheres are much smaller than the photon wavelength of the order of centimeters, so they can be treated as point particles. The static magnetic field $\mathbf{H}_{\rm app} = (0, H_{\rm app}, 0)$ in Fig. 1 is sufficiently strong to saturate the magnetization in the $\hat{\mathbf{y}}$ direction. The waveguide photons couple to the anticlockwise uniform magnetization precession around the magnetic field (Kittel mode). In second quantization $\hat{M}_{j,z} - i\hat{M}_{j,x} = \sqrt{2\hbar\gamma M_s/V_s}\hat{m}_j$, where $\hat{M}_{j,\delta}$ is the δth component of the magnetization amplitude in the jth magnet and $-\gamma$ the gyromagnetic ratio. Then the magnetic free energy $-\mu_0 \int [H_{\rm app}(\mathbf{r}) \hat{M}_y(\mathbf{r}) + \hat{\mathbf{H}}_{\rm eff}(\mathbf{r}) \cdot \hat{\mathbf{M}}(\mathbf{r})] d\mathbf{r}$, with effective magnetic field $\hat{\mathbf{H}}_{\rm eff}(\mathbf{r})$ generated by the dipolar and exchange interactions, reduces to that of a harmonic oscillator for each magnet $\hat{h}_{\rm m} = \hbar\omega_m \sum_{j=1}^N \hat{m}_j^\dagger \hat{m}_j$, where $\omega_m = \mu_0 \gamma H_{\rm app}$ is the Larmor precession frequency.

The photons and magnons are coupled by the Zeeman interaction $\hat{h}_{\rm int} = -\mu_0 \int \hat{\mathbf{H}}(\mathbf{r}) \cdot \hat{\mathbf{M}}(\mathbf{r}) d\mathbf{r}$, which here reduces to

$$\hat{h}_{\rm int} = \sum_j \int \frac{dk}{\sqrt{2\pi}} [\hbar g_j(k) \hat{p}_k \hat{m}_j^\dagger + \text{H.c.}]. \tag{1}$$

The coupling constant $g_j(k) = \tilde{g}(k) e^{ik(j-1)d}$, where

$$\tilde{g}(k) = -\mu_0 \sqrt{\frac{\gamma M_s V_s}{2\hbar}} [\mathcal{H}_{k,z}(\boldsymbol{\rho}) - i\mathcal{H}_{k,x}(\boldsymbol{\rho})], \tag{2}$$

depends on the position of the magnetic particles. Our treatment is perturbative in the sense that we disregard the disturbance of the waveguide fields by the magnetic spheres, which is a good approximation when the latter are sufficiently small [12].

The magnons interact resonantly with photons with wave numbers near $k_0 = \sqrt{\omega_m^2/c^2 - \pi^2/a^2}$. The magnetic field of TE photons is polarization-momentum locked; i.e., $\mathcal{H}_{k,-}$ depends on the sign of k [35–40] as worked out in the Supplemental Material for the TE_{10} mode [55]. A magnet at a position where $\mathcal{H}_{-k_0,-}$ is zero but $\mathcal{H}_{k_0,-}$ is finite can radiate only into the positive $\hat{\mathbf{z}}$ direction. For the TE_{10} mode this occurs for all y and $\cot(\pi x/a) = -\sqrt{k_0 a}\pi$.

Figure 2 is a snapshot of the magnetic-field distribution. The chiral lines for arbitrary cross sections [35] have to computed numerically.

The effective coupling between spheres can be modeled by integrating out the photon fields (for details, see Ref. [51]) in terms of the equation of motion for the vector of magnetizations $\hat{\mathcal{M}} = (\hat{m}_1, \ldots, \hat{m}_N)^T$ [56,57]:

$$d\hat{\mathcal{M}}/dt = -i\tilde{H}_{\rm eff}\hat{\mathcal{M}} - \hat{\mathcal{T}}. \tag{3}$$

$\hat{\mathcal{T}} = \hat{\mathcal{T}}_w + \hat{\mathcal{T}}_l$ is the external torque by the waveguide photons,

$$\hat{\mathcal{T}}_w = i \int \frac{dk}{\sqrt{2\pi}} \tilde{g}(k) \hat{p}_{k,\rm in} e^{-i\Omega_k t} (e^{ikd}, \ldots, e^{ikNd})^T, \tag{4}$$

and the local antennas $\hat{\mathcal{T}}_l = [\hat{P}_1(t), \ldots, \hat{P}_N(t)]^T$. In the non-Hermitian matrix $\tilde{H}_{\rm eff} = \tilde{\omega} + \Sigma$, $\tilde{\omega}_{jl} \equiv \tilde{\omega}_m \delta_{jl} = \omega_m(1 - i\alpha_G)\delta_{jl}$

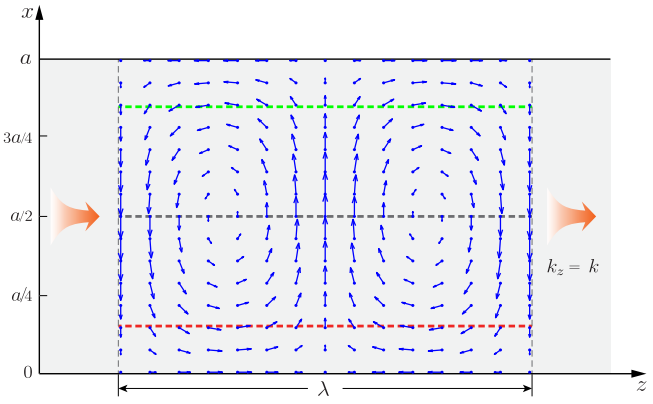

FIG. 2. Snapshot of magnetic-field vector distribution of the TE_{10} waveguide mode over one wavelength λ. The green and red dashed lines indicate the chiral lines with (opposite) circular polarization.

with Gilbert damping constant α_G, and the photon-mediated self-energy

$$\Sigma_{jl} = -i\begin{cases} (\Gamma_L+\Gamma_R)/2 & j=l \\ \Gamma_R e^{ik_0(j-l)d} & j>l \\ \Gamma_L e^{ik_0(l-j)d} & j<l, \end{cases} \tag{5}$$

where $\Gamma_R = \tilde{g}^2(k_0)/v(k_0)$, $\Gamma_L = \tilde{g}^2(-k_0)/v(k_0)$, and $v(k) = |k|c^2/\omega_m$ is the photon group velocity. The self-energy contributes to the dissipative and long-range coupling between any two magnets. The chiral coupling appears when $\Gamma_L \neq \Gamma_R$. The geometrical phases such as $k_0(j-l)d$ are caused by the photon propagating from the jth to the lth magnet. The modulus of the self-energy does not depend on distance because we assume sufficiently high quality of the waveguide and magnets.

Collective modes.—In the non-Hermitian Hamiltonian $\tilde{H}_{\rm eff}$, the right eigenvectors of Σ, say, $\{\psi_\zeta\}$ with corresponding eigenvalues $\{\gamma_\zeta\}$, satisfy $(\gamma_\zeta - \Sigma)\psi_\zeta = 0$ for a delocalized mode with label $\zeta \in \{1,\ldots,N\}$. Here $\mathrm{Re}[\gamma_\zeta]$ is the resonance frequency and $\mathrm{Im}[\gamma_\zeta]$ the reciprocal lifetime. $\{\psi_\zeta\}$ is normalized by $\psi_\zeta^T \mathcal{P}\psi_\zeta = 1$ with $\mathcal{P}_{ij} = \delta_{i+j,N}$ [23,58]. $\tilde{H}_{\rm eff}$ consists of a Hermitian $\tilde{H}_h = (\tilde{H}_{\rm eff} + \tilde{H}_{\rm eff}^\dagger)/2$ and non-Hermitian part $\tilde{H}_{nh} = (\tilde{H}_{\rm eff} - \tilde{H}_{\rm eff}^\dagger)/2$. $\hat{\mathcal{M}}$ can be expanded into generalized Bloch states $\hat{\Psi}_\kappa = \sum_{j=1}^N e^{i\kappa z_j}\hat{m}_j/\sqrt{N}$ with $z_j = (j-1)d$ and complex "crystal momentum" κ. Two Bloch states $\hat{\Psi}_{k_0}$ and $\hat{\Psi}_{-k_0}$ diagonalize $\tilde{H}_{nh}$ (recall $k_0 = \sqrt{\omega_m^2/c^2 - \pi^2/a^2}$):

$$\begin{pmatrix} \nu + \frac{i}{2}\Gamma_L N & \frac{i}{2}\Gamma_R \frac{1-e^{2ik_0Nd}}{1-e^{2ik_0 d}} \\ \frac{i}{2}\Gamma_L \frac{1-e^{-2ik_0Nd}}{1-e^{-2ik_0 d}} & \nu + \frac{i}{2}\Gamma_R N \end{pmatrix} \begin{pmatrix} \hat{\Psi}_{k_0} \\ \hat{\Psi}_{-k_0} \end{pmatrix} = 0. \tag{6}$$

The sum of the eigenvalues $\nu_+ + \nu_- = -iN(\Gamma_L+\Gamma_R)/2$ is the total radiative decay rate, which scales with number of magnets. These two states are called "superradiant" or "bright," while the remaining $(N-2)$ states are "subradiant" or "dark" with initially infinite radiative lifetime. The coherent coupling by $\tilde{H}_h$ mixes all states, but subradiant states with enhanced lifetimes persist, as shown below by combined analytic and numerical treatments.

The ansatz of extended Bloch states $\hat{\Psi}_\kappa$ leads to the closed expression for the Heisenberg equation [27]

$$d\hat{\Psi}_\kappa/dt = -i\omega_\kappa\hat{\Psi}_\kappa - \Gamma_L g_\kappa \hat{\Psi}_{k_0} + \Gamma_R h_\kappa \hat{\Psi}_{-k_0}, \tag{7}$$

in which

$$\omega_\kappa \equiv -i\frac{\Gamma_R}{2}\frac{1+e^{i(\kappa+k_0)d}}{1-e^{i(\kappa+k_0)d}} + i\frac{\Gamma_L}{2}\frac{1+e^{i(\kappa-k_0)d}}{1-e^{i(\kappa-k_0)d}}, \tag{8}$$

with $g_\kappa = 1/[1-e^{i(\kappa-k_0)d}]$ and $h_\kappa = e^{i(\kappa+k_0)Nd}/[1-e^{i(\kappa+k_0)d}]$. In an infinite chain (or a closed ring) $\hat{\Psi}_\kappa$ would be a solution. The boundary conditions of the finite system can be fulfilled by superposition of two states with momenta κ and κ' at the same frequency $\omega_\kappa = \omega_{\kappa'}$. The additional terms appearing in Eq. (7) are canceled by enforcing

$$g_\kappa h_{\kappa'} = g_{\kappa'} h_\kappa, \tag{9}$$

leading to eigenstates $\hat{\alpha}_\zeta = \sum_j \phi_{\zeta,j}^* \hat{m}_j \propto (g_\kappa \hat{\Psi}_{\kappa'} - g_{\kappa'}\hat{\Psi}_\kappa)$. The wave functions and spectra then read

$$\psi_{\zeta,j} \propto g_{\kappa'} e^{i\kappa z_{N-j}} - g_\kappa e^{i\kappa' z_{N-j}}, \qquad \gamma_\zeta = \omega_\kappa. \tag{10}$$

ω_κ diverges at $\kappa = \pm k_0$. On the other hand, the radiative damping $\sim \mathrm{Im}\omega_\kappa$ is minimized for, say, $\kappa = \kappa_*$. Neither $\kappa = \pm k_0$ nor κ_* solve Eq. (9), but these states reflect the superradiance and subradiance well known in quantum optics [26–31]. The former corresponds to the edge states of $\tilde{H}_{\rm eff}$ with enhanced magnon amplitudes and damping, while the latter are weakly coupled delocalized standing waves, as demonstrated in the following.

The wave numbers κ_* of the extremal points ω_{κ_*} lead to the vanishing group velocity around which the subradiant modes are expected, which obey

$$\kappa_* d = \arcsin\frac{\Gamma_R - \Gamma_L}{\sqrt{\Gamma_R^2 + \Gamma_L^2 - 2\Gamma_R\Gamma_L\cos(2k_0 d)}} - \arctan\frac{\Gamma_R - \Gamma_L}{(\Gamma_R+\Gamma_L)\tan(k_0 d)}. \tag{11}$$

$\arcsin x$ is a two-valued function in the first Brillouin zone $[-\pi/d, \pi/d]$ and we have two extremal points (see Supplemental Material [55]). The two degenerate solutions close to each extremum $\kappa_\pm = \kappa_* \pm \delta$ solve $g_{\kappa_+}h_{\kappa_-} = g_{\kappa_-}h_{\kappa_+}$. For small δ,

$$\delta_\zeta = \frac{\zeta\pi}{Nd}\left[1 - \frac{i}{N}\frac{\sin(k_0 d)}{\cos(\kappa_* d) - \cos(k_0 d)}\right], \tag{12}$$

where $\zeta \in N$. With Eq. (10), the wave function and dispersion of these subradiant states read

$$\psi_{\zeta,j} \approx -2i\frac{e^{i\kappa_* z_{N-j}}}{1-e^{i(\kappa_*-k_0)d}}\sin(\delta_\zeta z_{N-j}),$$
$$\omega_\zeta = \omega_{\kappa_*} + \frac{\sin(k_0 d)}{\cos(\kappa_* d) - \cos(k_0 d)}\frac{\Gamma_R(\delta_\zeta d)^2/2}{1-\cos[(k_0+\kappa_*)d]}, \tag{13}$$

where $\delta_\zeta \propto \zeta/(Nd)$. These solutions are nearly standing waves with long radiative lifetimes and are only weakly affected by chirality.

We have to numerically calculate the solutions for κ close to $\pm k_0$, i.e., $\kappa = k_0 + \eta$ and $\kappa' = -k_0 + \eta'$, in which η and η' are small complex numbers. $\mathrm{Im}\,\eta$ and $\mathrm{Im}\,\eta'$ govern the decay of the states at the two edges. With chirality, only one of them is important, which causes a concentration at one edge of the chain.

As an example, we consider a rectangular waveguide with dimensions $a = 1.6$ cm and $b = 0.6$ cm, and 20 YIG magnetic spheres with radius $r_c = 0.6$ mm and $\alpha_G = 5 \times 10^{-5}$ [54]. $\omega_m/(2\pi) = \sqrt{3}c/(2a) = 16.2$ GHz is tuned to correspond to the photon momentum $k_0 = \sqrt{2}\pi/a$ of the lowest TE_{10} mode. By varying the position and size of the magnets, we may tune the magnon-photon interaction Eq. (5), here $\Gamma_{R,L}/(2\pi) \in (0, 20)$ MHz, while $\alpha_G\omega_m/(2\pi) \sim 1$ MHz and chiralities $0 < \Gamma_L/\Gamma_R < \infty$. $k_0 d = 3\pi/5$ corresponds to an intermagnet spacing $d = a/(5\sqrt{2}) \approx 0.6$ cm and $Nd \approx 12$ cm.

Magnon accumulation.—Figure 3 is a plot of the energy spectra and magnon accumulation (squared wave functions). Figure 3(a) shows that the real and imaginary components of the eigenenergy γ_ζ, scaled by $\Gamma_a = (\Gamma_L + \Gamma_R)/2$, are approximately distributed on an ellipse in the complex plane that depends only weakly on the chirality. The solutions with long lifetimes are clustered around the frequencies ω_{κ_*}. It is negative in Fig. 3(a) but depends strongly on k_0. Modes with $\mathrm{Im}\gamma > \Gamma_a$ ($< \Gamma_a$) are superradiant (subradiant) with radiative lifetime shorter (longer) than that of an isolated magnet. The decay rates of all eigenstates are sorted and plotted with integer labels $\zeta \in \{1, 2, \ldots, 20\}$ in Fig. 3(b). Here, the typical radiative lifetime of the most superradiant state ($\zeta = 20$) is 20–70 MHz for the three chiralities.

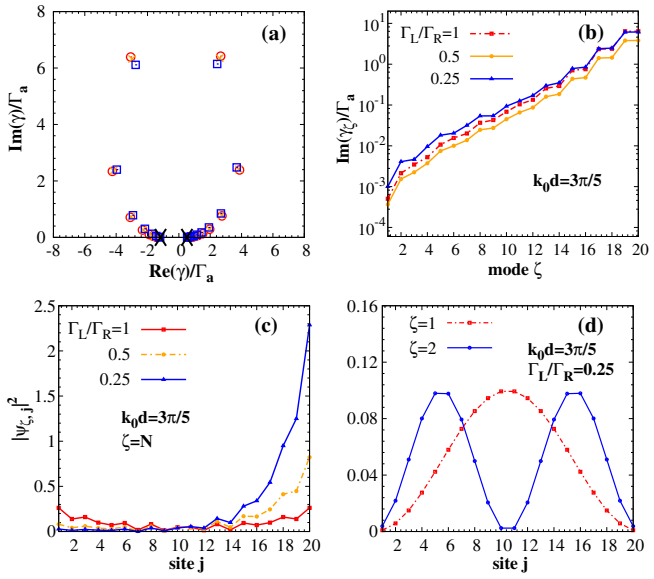

FIG. 3. Energy spectra and wave functions of the magnet chain. (a) Real and imaginary components of eigenenergies $\gamma = (\nu - \tilde{\omega}_m)$ scaled by $\Gamma_a = (\Gamma_L + \Gamma_R)/2$. Red circles, orange crosses, and blue squares encode the chiralities $\Gamma_L/\Gamma_R = 1$, 0.5, and 0.25, respectively. Black crosses indicate two values of $\omega_{\kappa_*}/\Gamma_a$ when $\Gamma_L/\Gamma_R = 0.25$. (b) All 20 eigenstates sorted by increasing decay rates. (c) Magnon intensity distribution of the most short-lived state with $\zeta = 20$ in (b). (d) Magnon intensity distribution for the longest living states with $\zeta = 1$, 2 in (b).

The magnon accumulation $|\psi_{\zeta,j}|^2$ of the most short-lived state [$\zeta = 20$ in Fig. 3(b)] is plotted in Fig. 3(c). When $\Gamma_R = \Gamma_L$, the state is symmetrically localized close to both edges (red solid curve), but with increasing chirality, the distribution becomes asymmetrically skewed to one boundary. When $\Gamma_R < \Gamma_L$ ($\Gamma_R > \Gamma_L$), the boundary state is localized at the left (right) boundary of the chain. The enhanced dynamics associated to large magnon numbers causes superradiance. The most subradiant states, on the other hand, have magnon accumulations $\sim|\sin(\zeta\pi j/N)|^2$, with small amplitudes at the two boundaries, as shown in Fig. 3(d), and are only weakly affected by chirality. A weak higher harmonic reflects the bare photon wavelength $\sim 2\pi/k_0$.

We can now expand the magnetization $\hat{\mathcal{M}}(t) = \sum_{\zeta=1}^{N} \hat{\alpha}_\zeta(t)\psi_\zeta$ into the above eigenstates with coefficients $\hat{\alpha}_\zeta(t) = \phi_\zeta^\dagger \hat{\mathcal{M}}(t)$. For the local input vector at common frequency ω_{in}, $\langle \hat{\mathcal{T}}_l(t)\rangle = ie^{-i\omega_{\mathrm{in}}t}(P_1, P_2, \ldots, P_N)$ and waveguide photon feed $\langle \hat{\mathcal{T}}_w\rangle = 0$ (we discuss the case with $\langle \hat{\mathcal{T}}_w\rangle \neq 0$ and $\langle \hat{\mathcal{T}}_l\rangle = 0$ in Ref. [51]), the coherent magnetization amplitude

$$\langle \hat{\mathcal{M}}(t)\rangle = -i\sum_\zeta \frac{(\mathcal{P}\psi_\zeta)^T\langle \hat{\mathcal{T}}_l(t)\rangle}{\omega_{\mathrm{in}} - \tilde{\omega}_m - \gamma_\zeta}\psi_\zeta. \tag{14}$$

We are looking for a large magnon accumulation at one edge of the chain due to the chirality. Since $(\mathcal{P}\psi_\zeta)^T = (\psi_{\zeta,N}, \psi_{\zeta,N-1}, \ldots, \psi_1)$ oscillates between spheres with fixed phase, the vector product $(\mathcal{P}\psi_\zeta)^T\langle \hat{\mathcal{T}}_l(t)\rangle$ can be large for a localized edge state ζ_* on the right when the input from the local antennas matches its phase and frequency. To match the phases of the edge states, we consider local power injection of the form $\langle \hat{\mathcal{T}}_l(t)\rangle = iP(1, e^{i\phi}, \ldots, e^{i(N-1)\phi})\exp[-i(\omega_m + \mathrm{Re}\gamma_{\zeta_*})t]$, in which the optimal phase depends on the number of magnets but $\phi \to k_0 d$ for sufficiently long chains.

Figure 4(a) shows that switching on the local antennas for $\Gamma_L/\Gamma_R = 0.1$ and phase ϕ optimally chosen to be $\sim 0.35\pi$ leads to an enhanced accumulation on the right side. This choice of ϕ is out of phase with the subradiant states that are therefore hardly excited [see the blue curve in Fig. 4(a)]. Figure 4(b) is the accumulation on the rightmost sphere as a function of chirality, which is enhanced more than 100-fold by tuning the chirality $\Gamma_L/\Gamma_R \to 0$. In this limit all frequencies become degenerate, but individual modes can still be accessed by the phased array. With fixed chirality, the amplitude $|M_N|$ of the edge state with $\zeta = N$ diverges with the number of magnets as $\propto \sqrt{N}$. On the other hand, this state is also superradiant, with lifetime that decreases with the number of magnets, approximately $\propto 1/N$. Therefore, with fixed power input per coil, the accumulated magnetization $|M_N|$ at the boundary is estimated to be constant, while the calculations show a slow decrease with N [55].

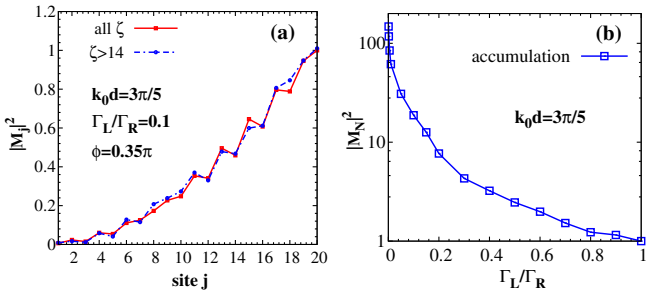

FIG. 4. Magnon accumulation excited by a phased antenna array with $N = 20$ magnets. (a) The accumulation (squared magnetization amplitude) distribution over the magnets (red curve) is normalized by the largest value at the edge. The blue curve excludes the contribution of subradiant states. (b) Magnon accumulation as a function of chirality, normalized by its value for $\Gamma_L/\Gamma_R = 1$.

Conclusions.—In conclusion, the interaction between magnons and photons can be chiral and tunable by strategically positioning small magnets in a waveguide. We predict a strong imbalance of magnon populations in a chain of magnets in which the dissipative and long-range nature of the coupling can strongly enhance the magnon intensity at the edges that can be much higher than those excited by conventional ferromagnetic resonance. On the other hand, the magnon numbers of the magnets in the center of the chain are only weakly affected.

Our formalism can be extended into the quantum regime of magnons [26–30]. The strong coupling between magnons and photons in a microwave waveguide [54] opens the new perspective of magnonic quantum emitters [59], which might help circumventing the harsh experimental environment such as extremely low temperature and fine control required for cold atom system. We also find analogies with chiral optics, in which the coupling between light and emitters depends on the propagation of light and polarization of the local emitters [36]. The chiral coupling between emitters is promising in achieving quantum state transfer between qubits via the magnonic chiral quantum channel introduced here.

This work is financially supported by the Nederlandse Organisatie voor Wetenschappelijk Onderzoek (NWO) as well as JSPS KAKENHI (Grant No. 19H006450). Y.-X. Z. is supported by the European Union's Horizon 2020 research and innovation program (Grant No. 712721, NanOQTech).

[1] A. Auerbach, *Interacting Electrons and Quantum Magnetism* (Springer-Verlag, New York, 1994).
[2] M. A. Ruderman and C. Kittel, Phys. Rev. **96**, 99 (1954); T. Kasuya, Prog. Theor. Phys. **16**, 45 (1956); K. Yosida, Phys. Rev. **106**, 893 (1957).
[3] H. Suhl, Phys. Rev. **109**, 606 (1958).
[4] T. Nakamura, Prog. Theor. Phys. **20**, 542 (1958).
[5] L. Mandel and E. Wolf, *Optical Coherence and Quantum Optics* (Cambridge University Press, Cambridge, England, 1995).
[6] Ö. O. Soykal and M. E. Flatté, Phys. Rev. Lett. **104**, 077202 (2010).
[7] H. Huebl, C. W. Zollitsch, J. Lotze, F. Hocke, M. Greifenstein, A. Marx, R. Gross, and S. T. B. Goennenwein, Phys. Rev. Lett. **111**, 127003 (2013).
[8] Y. Tabuchi, S. Ishino, T. Ishikawa, R. Yamazaki, K. Usami, and Y. Nakamura, Phys. Rev. Lett. **113**, 083603 (2014).
[9] X. Zhang, C.-L. Zou, L. Jiang, and H. X. Tang, Phys. Rev. Lett. **113**, 156401 (2014).
[10] X. Zhang, C.-L. Zou, N. Zhu, F. Marquardt, L. Jiang, and H. X. Tang, Nat. Commun. **6**, 8914 (2015).
[11] N. J. Lambert, J. A. Haigh, S. Langenfeld, A. C. Doherty, and A. J. Ferguson, Phys. Rev. A **93**, 021803(R) (2016).
[12] B. Zare Rameshti and G. E. W. Bauer, Phys. Rev. B **97**, 014419 (2018).
[13] N. Hatano and D. R. Nelson, Phys. Rev. Lett. **77**, 570 (1996).
[14] C. M. Bender, D. C. Brody, and H. F. Jones, Phys. Rev. Lett. **89**, 270401 (2002).
[15] C. M. Bender, D. C. Brody, H. F. Jones, and B. K. Meister, Phys. Rev. Lett. **98**, 040403 (2007).
[16] D. Zhang, X.-Q. Luo, Y.-P. Wang, T.-F. Li, and J. Q. You, Nat. Commun. **8**, 1368 (2017).
[17] R. El-Ganainy, K. G. Makris, M. Khajavikhan, Z. H. Musslimani, S. Rotter, and D. N. Christodoulides, Nat. Phys. **14**, 11 (2018).
[18] S. Y. Yao and Z. Wang, Phys. Rev. Lett. **121**, 086803 (2018).
[19] Z. Gong, Y. Ashida, K. Kawabata, K. Takasan, S. Higashikawa, and M. Ueda, Phys. Rev. X **8**, 031079 (2018).
[20] X. S. Yang, Y. Cao, and Y. Zhai, arXiv:1904.02492.
[21] S. Y. Yao, F. Song, and Z. Wang, Phys. Rev. Lett. **121**, 136802 (2018).
[22] H. Jiang, L. J. Lang, C. Yang, S. L. Zhu, and S. Chen, Phys. Rev. B **100**, 054301 (2019).
[23] N. Moiseyev, *Non-Hermitian Quantum Mechanics* (Cambridge University Press, Cambridge, England, 2011).
[24] M. Harder, Y. Yang, B. M. Yao, C. H. Yu, J. W. Rao, Y. S. Gui, R. L. Stamps, and C.-M. Hu, Phys. Rev. Lett. **121**, 137203 (2018).
[25] B. M. Yao, T. Yu, X. Zhang, W. Lu, Y. S. Gui, C.-M. Hu, and Y. M. Blanter, Phys. Rev. B **100**, 214426 (2019).
[26] A. Asenjo-García, M. Moreno-Cardoner, A. Albrecht, H. J. Kimble, and D. E. Chang, Phys. Rev. X **7**, 031024 (2017).
[27] Y.-X. Zhang and K. Mølmer, Phys. Rev. Lett. **122**, 203605 (2019).
[28] M. Moreno-Cardoner, D. Plankensteiner, L. Ostermann, D. E. Chang, and H. Ritsch, Phys. Rev. A **100**, 023806 (2019).
[29] P.-O. Guimond, A. Grankin, D. V. Vasilyev, B. Vermersch, and P. Zoller, Phys. Rev. Lett. **122**, 093601 (2019).
[30] G. Buonaiuto, R. Jones, B. Olmos, and I. Lesanovsky, arXiv:1902.08525.
[31] J. Li, S. Y. Zhu, and G. S. Agarwal, Phys. Rev. Lett. **121**, 203601 (2018).

[32] L. M. Sieberer, S. D. Huber, E. Altman, and S. Diehl, Phys. Rev. Lett. **110**, 195301 (2013).

[33] S. Diehl, A. Micheli, A. Kantian, B. Kraus, H. P. Büchler, and P. Zoller, Nat. Phys. **4**, 878 (2008).

[34] N. R. Bernier, E. G. Dalla Torre, and E. Demler, Phys. Rev. Lett. **113**, 065303 (2014).

[35] J. D. Jackson, *Classical Electrodynamics* (Wiley, New York, 1998).

[36] P. Lodahl, S. Mahmoodian, S. Stobbe, A. Rauschenbeutel, P. Schneeweiss, J. Volz, H. Pichler, and P. Zoller, Nature (London) **541**, 473 (2017).

[37] F. Le Kien, S. Dutta Gupta, K. P. Nayak, and K. Hakuta, Phys. Rev. A **72**, 063815 (2005).

[38] B. le Feber, N. Rotenberg, and L. Kuipers, Nat. Commun. **6**, 6695 (2015).

[39] M. Scheucher, A. Hilico, E. Will, J. Volz, and A. Rauschenbeutel, Science **354**, 1577 (2016).

[40] B. Vermersch, P.-O. Guimond, H. Pichler, and P. Zoller, Phys. Rev. Lett. **118**, 133601 (2017).

[41] A. G. Gurevich, Radiotekh. Elektron. (Moscow) **8**, 780 (1963).

[42] A. G. Gurevich and G. A. Melkov, *Magnetization Oscillations and Waves* (CRC, New York, 1996).

[43] L. Martin, U.S. Patent No. US3426297A (1966).

[44] V. S. L'vov, *Wave Turbulence Under Parametric Excitations: Applications to Magnetics* (Springer, Berlin, 1994).

[45] T. Yu, C. P. Liu, H. M. Yu, Y. M. Blanter, and G. E. W. Bauer, Phys. Rev. B **99**, 134424 (2019).

[46] J. L. Chen, T. Yu, C. P. Liu, T. Liu, M. Madami, K. Shen, J. Y. Zhang, S. Tu, M. S. Alam, K. Xia, M. Z. Wu, G. Gubbiotti, Y. M. Blanter, G. E. W. Bauer, and H. M. Yu, Phys. Rev. B **100**, 104427 (2019).

[47] T. Yu, Y. M. Blanter, and G. E. W. Bauer, Phys. Rev. Lett. **123**, 247202 (2019).

[48] Y. Tserkovnyak, A. Brataas, G. E. W. Bauer, and B. I. Halperin, Rev. Mod. Phys. **77**, 1375 (2005).

[49] A. Kamra, H. Keshtgar, P. Yan, and G. E. W. Bauer, Phys. Rev. B **91**, 104409 (2015).

[50] S. Streib, H. Keshtgar, and G. E. W. Bauer, Phys. Rev. Lett. **121**, 027202 (2018).

[51] T. Yu, X. Zhang, S. Sharma, Y. M. Blanter, and G. E. W. Bauer, companion paper, Phys. Rev. B **101**, 094414 (2020).

[52] U. Fano, Phys. Rev. **124**, 1866 (1961).

[53] G. D. Mahan, *Many Particle Physics* (Plenum, New York, 1990).

[54] B. M. Yao, T. Yu, Y. S. Gui, J. W. Rao, Y. T. Zhao, W. Lu, and C.-M. Hu, Commun. Phys. **2**, 161 (2019).

[55] See Supplemental Material at http://link.aps.org/supplemental/10.1103/PhysRevLett.124.107202 for expression of normalized TE_{10} eigenmode and detailed explanations of collective superradiant modes.

[56] C. W. Gardiner and M. J. Collett, Phys. Rev. A **31**, 3761 (1985).

[57] A. A. Clerk, M. H. Devoret, S. M. Girvin, F. Marquardt, and R. J. Schoelkopf, Rev. Mod. Phys. **82**, 1155 (2010).

[58] $\{\phi_\zeta\} \neq \{\psi_\zeta\}$ are the eigenvectors of $\Sigma^\dagger$ with eigenvalues $\{\gamma_\zeta^*\}$. In the absence of degeneracies in $\{\gamma_\zeta\}$ the (normalized) modes are "biorthonormal"; i.e., $\phi_\zeta^\dagger \psi_{\zeta'} = \delta_{\zeta\zeta'}$ [26]. With $\Sigma^\dagger = \mathcal{P}\Sigma^*\mathcal{P}$, where $\mathcal{P}_{ij} = \delta_{i+j,N}$ inverts the order of magnets $1 \leftrightarrow N$, $2 \leftrightarrow N-1$, …, we arrive at $\phi_\zeta = \mathcal{P}\psi_\zeta^*$ [51].

[59] V. E. Demidov, S. Urazhdin, G. de Loubens, O. Klein, V. Cros, A. Anane, and S. O. Demokritov, Phys. Rep. **673**, 1 (2017).